



# New insights into sono-exfoliation mechanisms of graphite: In situ high-speed imaging studies and acoustic measurements

Justin A. Morton<sup>1,\*</sup>, Mohammad Khavari<sup>1,2</sup>, Ling Qin<sup>3</sup>, Barbara M. Maciejewska<sup>2</sup>, Anastasia V. Tyurnina<sup>4</sup>, Nicole Grobert<sup>2,7</sup>, Dmitry G. Eskin<sup>4</sup>, Jiawei Mi<sup>3</sup>, Kyriakos Porfyrakis<sup>5</sup>, Paul Prentice<sup>6</sup>, Iakovos Tzanakis<sup>1,2</sup>

<sup>1</sup> School of Engineering, Computing and Mathematics, Oxford Brookes University, College Ct, Wheatley, Oxford OX33 1HX, UK

<sup>2</sup> Department of Materials, University of Oxford, Parks Road, Oxford OX1 3PH, UK

<sup>3</sup> Department of Engineering, University of Hull, Cottingham Rd, Hull HU6 7RX, UK

<sup>4</sup> Brunel Centre for Advanced Solidification Technology, Brunel University London, Kingston Lane, UB8 3PH, UK

<sup>5</sup> Faculty of Engineering and Science, University of Greenwich, Central Avenue, Chatham Maritime, Kent ME4 4TB, UK

<sup>6</sup> Cavitation Laboratory, School of Engineering, University of Glasgow, University Avenue, G128QQ, UK

<sup>7</sup> Williams Advanced Engineering, Grove, Oxfordshire OX12 0DQ, UK

The application of ultrasound and acoustic cavitation in liquid exfoliation of bulk layered materials is a widely used method. However, despite extensive research, the fundamental mechanisms remain far from being fully understood. A number of theories have been proposed to interpret the interactions between cavitation and bulk layered materials and hence to explain the mechanisms of ultrasound assisted exfoliation. Unfortunately, most of the research reported to date is ambiguous or inconclusive due to lack of direct real-time experimental evidence. In this paper, we report systematic work characterising cavitation emissions and observing the exfoliation of graphite in situ, in deionised water under the dynamic interaction with laser and ultrasound induced cavitation bubbles. Using ultra-high-speed optical imaging, we were able to determine the dynamic sequence of graphite exfoliation events on a time scale never reported before. Real-time observations also revealed that shock waves with a pressure magnitude up to 5 MPa and liquid-jets in the range of  $80 \text{ ms}^{-1}$ , from transient cavitation bubble implosions, were essential for the initiation and propagation of the exfoliation process. On the other hand, bubble oscillations associated with stable cavitation were beneficial for promoting a gentler delamination of graphite layers.

**Keywords:** Ultrasonic exfoliation; Sono-exfoliation; Cavitation; Shock wave; Liquid-jet; Acoustic streaming; Graphene; Bubble dynamics

## Introduction

Since the discovery of graphene in 2004 by Novoselov et al. [1], there has been an immense amount of interest and a plethora of research into the exfoliation of bulk layered materials, their properties, production methods and applications [2–7]. In partic-

ular, liquid phase exfoliation (LPE) has been demonstrated to be an effective method of producing high quality two dimensional (2D) materials with large surface areas, which can therefore be used for a wide variety of applications [8]. The most challenging issue concerning LPE is the yield and production efficiency as well as the use of toxic solvents and surfactants in order to facilitate delamination and stabilisation of the layered materials. These

\* Corresponding author.

E-mail address: Morton, J.A. (18096707@brookes.ac.uk)

environmentally harmful solvents can be expensive and also present problems with their removal during nanosheet (typically 1–100 nm) collection, which in turn reduces the number of material applications [9]. To this end, the use of ultrasonication in combination with pure water as an ideal solvent has been proposed to facilitate exfoliation of layered materials. Recent research supports the proposal, demonstrating this combination under controlled ultrasonication parameters to promote high quality graphene flakes in a relatively short period of time [10,11].

Ultrasonic processing is a cost effective and energy efficient technique that uses the dynamics of cavitation bubbles to supply the necessary shear forces for exfoliation (sono-exfoliation). Cavitation bubbles were previously shown to be capable of generating high-speed liquid-jets exceeding  $100 \text{ ms}^{-1}$  [12,13] and local hydrodynamic impact pressures up to 1 GPa, which have been regarded sufficient to promote rapid exfoliation of bulk layered materials [14]. However, such exfoliation events have yet to be observed in situ, and sono-exfoliation mechanisms have only been suggested based on post-treatment analysis [5,15]. Only very recently, experimental evidence from acoustic pressure measurements indirectly indicated that transient cavitation (associated with shock wave (SW) generation) is the main driving exfoliation mechanism in a sonicated environment [11]. On the other hand, a recent numerical approach revealed that the initiation of exfoliation is predicated on initial large shear forces from nano-jets (generated during bubble implosion), subsequently followed by tensile stresses from reflected SWs facilitating delamination of the surface layers, by overcoming the Van der Waals (VdW) forces [16]. These studies place emphasis on the contribution of SWs to sono-exfoliation, although the lack of in situ experimental evidence due to the inherent difficulties in capturing the real dynamic events in real-time, impose validation restrictions and limits our understanding, and consequently optimization and scale up of this promising process.

In this study we took the next step with advanced in situ observations of the sono-exfoliation process complemented by numerical modelling and in situ measurements of the acoustic pressure field. We thoroughly studied the exfoliation mechanisms of graphite flakes subjected to laser induced bubbles (LIB) (spatiotemporally controlled cavitation collapses) and acoustic cavitation (multiple uncontrolled bubble collapses/sonicated environment). We investigated the role of different types of cavitation bubbles (transient and stable cavitation) in the exfoliation process, and elucidated their respective importance and contribution. Results of direct in situ experiments and camera observations made it apparent that there are multiple “manifestations” of exfoliation occurring, which have not been previously thought about. The next sections will analyse each of these newly identified manifestations in detail. Due to the benefits of developing a large scale environmentally friendly exfoliation process, all experiments were performed in deionised water as the prime liquid medium.

## Results and discussion

### Single laser induced bubble experiments

By focusing a laser beam, plasma is created within the liquid medium, which rapidly expands to form a growing cavity [17–

19]. One of the benefits of producing cavitation through this method is that the position of the cavity can be easily determined and controlled, unlike the inherently stochastic nature of forming inertial bubbles from a sonotrode. In the latter case, bubble dynamics are difficult to discern due to the number of cavities formed. Moreover, by removing the uncertainties such as observing multibubble clouds, and knowing where and when a cavitation bubble will form, we could use a high-speed camera to capture high-definition and exceptionally high-frame-rate images capable of resolving these interactions and dynamics. For this study, individual bubble interactions including shock waves, liquid jets as well as oscillatory effects of stable bubbles with graphite flakes provided a much more controlled observation and enabled the analysis of sono-exfoliation mechanisms occurring in response to acoustic cavitation.

Both types of cavitation bubbles; transient (rapidly changing bubble diameter with implosion) and stable (higher stability bubbles, pulsating for longer periods of time) were found to contribute to the exfoliation of the studied graphite flakes. In particular, the implosion of bubbles located just above the top of the graphite flake, aligning to the in-plane direction of the bonded inter-graphitic layers, was found to be effective. The orientation of the graphite flakes in this report were designed to promote scissions into the graphite layers and, hence, the samples were fixed vertically onto the metallic holder with adhesive. Evidently, this would not necessarily be the case in an uncontrolled or industrial scenario, however, the practicality of this report was to investigate and elucidate the fundamental mechanisms that promote and facilitate exfoliation, and propose optimised setups and sonication parameters leading to more efficient treatment. The experimental setup for the LIBs can be found in [Supplementary Material Fig. S1\(a\)](#).

### Exfoliation via transient cavitation

[Fig. 1](#) demonstrates how the surface area of the graphite flake tip expanded ([Fig. 1\(d1\)](#)) from consecutive bubble implosions at the point of impact, which occurred at a distance between 0.8–1.25 mm above the graphite flake tip, ensuring contactless interaction, i.e. resulting in only SW interactions with the studied samples. Multiple SW fronts were recorded interacting with the graphite, promoting exfoliation in a manner resembling that of a flower blooming. This “flowering” manifestation appeared to constitute an initial stage of separation of layers at the graphite tip, hence widening the top of the graphite flake with force exerted by powerful SWs. Numerical modelling generated via the 2D volume of fluid method (VOF) was used to provide estimates for LIB in situ measurements. These consisted of using specific bubble parameters for each experiment case. More information on these models can be found in Method (Section 4) and [Supplementary Material Section 2](#). SW impacts based on parameters from [Fig. 1](#) were estimated to emit pressures in a range of ~0.45 to 1.2 MPa depending on their initial distance away from the graphite sample (shown in [Fig. S2](#)). The temporal accumulations of these impacts were shown to drastically change the morphology of the graphite flake.

Initially, the thickness at the tip of the graphite flake was ~0.28 mm ([Fig. 1\(a1\)](#)), 30 LIBs later ([Fig. 1\(d1\)](#)) the graphite flake thickness at the tip increased to ~0.71 mm. Consequently, in

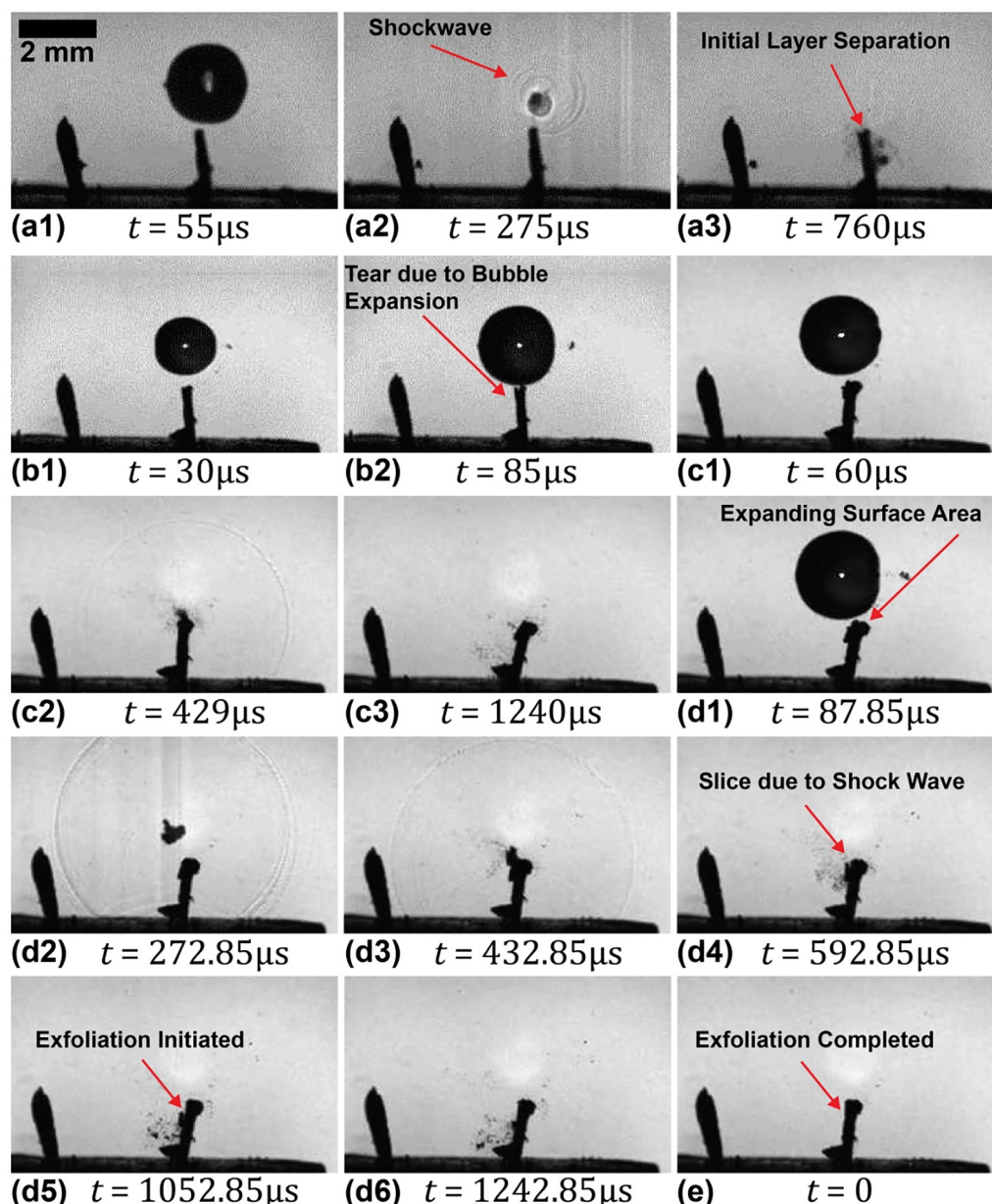


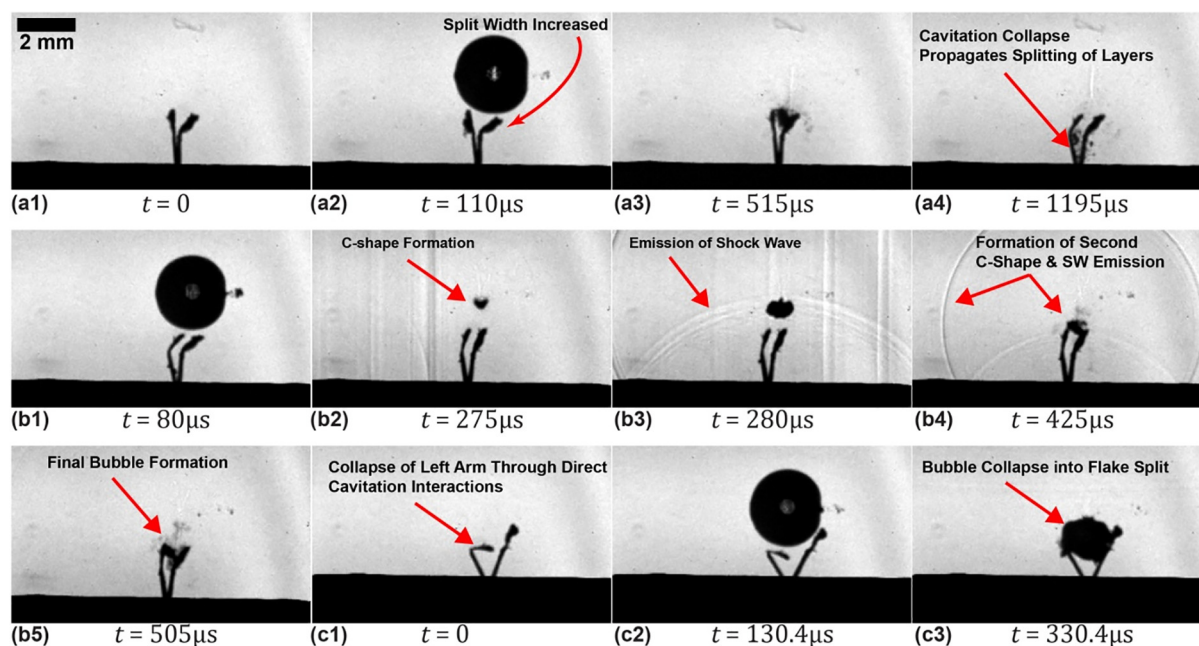
FIGURE 1

Representative frames selected from multiple high-speed sequences (separated by letter) recording the interaction of repeated LIBs with a single graphite flake, depicting the “flowering” manifestation. **(a1-3)** An expanding LIB forms above the graphite flake (1). The bubble collapse generates a SW which interacts with the graphite flake tip (with a vertical reflected SW also seen on the right hand side) (2). A split is initiated due to the shear forces exerted by the SWs (3). **(b1-2)** An expanding LIB (1) pushes the graphite flake tip apart making the initiated split noticeably visible (2). **(c1-3)** After 16 more LIBs, the graphite flake tip surface area expands resembling a “flower” shape (1). A subsequent LIB collapses emitting SWs (2) which continue to widen the tip surface area. The graphite flake base is also seen to lift in position due to LIB interactions (3). **(d1-5)** Another LIB forms (1) and collapses propagating SWs towards the graphite flake (2). The post-collapse rebound generates a secondary SW closer to the graphite flake tip (3), which induces a small perceptible split to the graphite layers (4). Exfoliation takes place as the forces keeping the graphite layers in tact are superseded (5) (video 1). The delaminated graphite flake sinks towards the substrate (5). **(e)** The final flake morphology.

**Fig. 1(d5)** the newly generated cavitation bubble imploded and SWs interacted with the already expanded graphite flake tip. At this point the weakened section of  $\sim 360\ \mu\text{m}$  in length and  $\sim 120\ \mu\text{m}$  in thickness separated from the flake, drifted away and sedimented in water. This cutting or “slicing” manifestation occurred when a crack or small pit was initiated due to the accumulative shock wave impacts, followed by a sharp scission straight through a section of the graphite flake in the direction

parallel to the bonded inter-layers. A more detailed explanation alongside high-speed images can be found in the [Supplementary Material Section 2 Fig. S3](#).

From this series of observations it was apparent that the “flowering” manifestation opened up the tip of the graphite flake, essentially weakening the structure (breaking/relaxing the bonds) generally across the whole graphite tip followed by exfoliation of a section via the “slicing” manifestation, typically

**FIGURE 2**

Representative frames selected from multiple high-speed sequences (separated by letter) recording the interaction of repeated LIBs with a single graphite flake, depicting the “splitting” manifestation. **(a1-4)** A graphite flake, already split through previous interactions (1), displays further splitting as another LIB reaches maximum expansion (2). The bubble deflates and translates into the split, propagating it further (3). The post-collapse rebound completes the split along the length of the graphite flake (4) (Video 2). **(b1-5)** A subsequent LIB at maximum expansion bends the open end of the split (1), deflates into a c-shape indicative of jetting (2) and generates a multi-fronted SW, reflecting from the substrate, on collapse (3). The rebounding bubble also deflates to form a c-shape and collapses to generate a secondary SW (4). The bubble collapses directly into the split (5). **(c1-3)** After 5 more LIBs the graphite flake component layers have thinned, one to the point of flexure (1), with further bubbles widening the split at maximum expansion (2), in addition to collapse and rebounds (3).

within 30 ms of accumulated LIB interaction time. In addition, although the graphite flake was seen to expand due to the separation of layers, in the microscopic level it is likely that micro-exfoliation was also occurring as discussed in relevance to [Supplementary Material Section 2 Fig. S4\(c-d\)](#).

Apart from the SWs, liquid-micro jets were found to play an important role in promoting exfoliation of the graphite flakes. [Fig. 2](#) shows a LIB imploding at a distance between 0.72 and 1.38 mm from the fixed graphite flake which had already been half split intentionally by a previous cavitation interaction, in order to investigate the “wedge” effect phenomenologically described by Yi et al. [20]. During the bubble collapse phase a C-shape (or involution) cavitation vortex forms. Although micro-jetting cannot be resolved, the C-shape indicates the preliminary stage of the liquid-jet formation and has been reported on many occasions [14,21,22]. Water entrainment occurred from the back of the bubble, where liquid mass was pulled through and propelled towards the half-split section with high velocities approximately  $80 \text{ ms}^{-1}$  as calculated using the images from the high-speed camera (see [Fig. S5](#)). When this high momentum liquid mass interacted with the sample surface, large impact pressure forces in the MPa range [14] were inflicted onto the layers promoting further splitting, hence our terminology for the “splitting” manifestation. Eventually, and after 9 consecutive bubble collapses ([Fig. 2\(a4\)](#)), the graphite flake was fully split down the centre with thinning becoming more prevalent. The final images ([Fig. 2\(c1-c2\)](#)) show that the accumulation of collapses was burgeoning the peeling of graphite layers. The gra-

phite flake morphology was significantly altered with the split flake arms wedged further apart.

We observed that exfoliation via transient cavitation tends to manifest in three ways, “flowering” “slicing” and “splitting”. [Fig. 3](#) displays a schematic representation of these manifestations. As previously mentioned, the graphite flake tip widens due to SW impacts ([Fig. 3\(b1\)](#)), followed by exfoliation ([Fig. 3\(c1\)](#)). Defects at the tip of the graphite flake, or weakened bonds at a specific point have the propensity to facilitate the “slicing” manifestation. Alternatively, liquid-jets propelled into the graphite flake surface ([Fig. 3\(b2\)](#)) can expedite exfoliation by rapidly tearing through layers (“splitting”) with bubble rebounds. After the cavity can no longer rebound being wedged between the two splitting arms, bubble fragments remain and dissipate ([Fig. 3\(c2\)](#)). In a continuous sonicated environment, these bubble fragments can play the role of tiny nuclei that can be excited by the both the sonication and bubble-collapse SWs from the cavitation activity in the liquid. This could drive the intra-flake nuclei to further collapses and micro-jetting, or sustain a more stable regime with vigorous oscillations, with both cases further contributing to exfoliation [23].

#### Exfoliation via stable cavitation

As opposed to the current views that stable cavitation is ineffective for the delamination of bulk layered materials, we show for the first time that bubble oscillation does indeed play a crucial role in the exfoliation process. In the situation where the LIBs were now located at either side of the graphite flake ([Fig. 4](#), LIB



## Exfoliation via Transient Cavitation

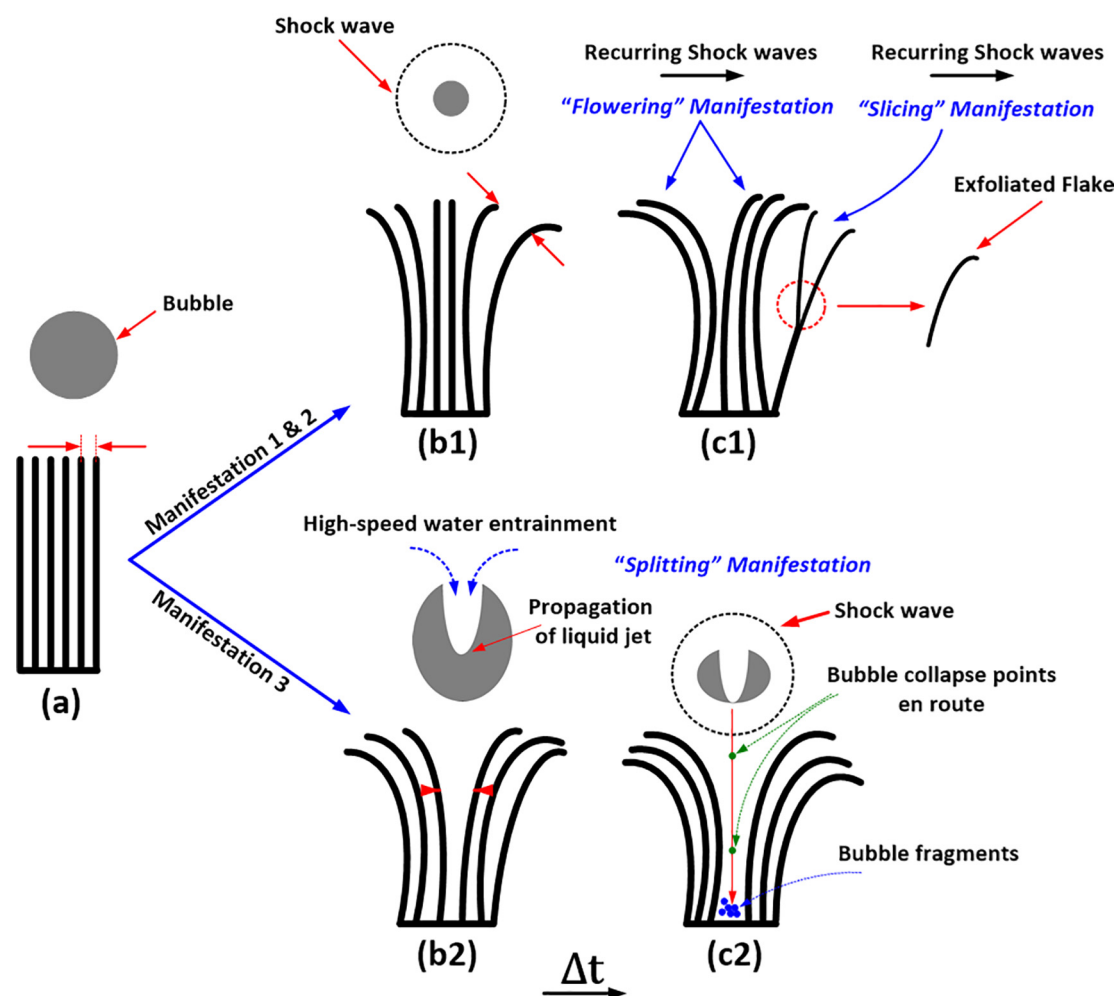


**FIGURE 3**

Schematic portraying a transient cavitation interaction with a graphite flake whereby three sono-exfoliation manifestations can take place (1 “flowering”, 2 “slicing”, 3 “splitting”). **(a)** Initially the layers are unaffected, bound by VdW’s forces and closely attached vertically (where each black pillar represents  $\sim 50 \mu\text{m}$  thickness of graphite). **(b1)** Multiple SWs interact with the graphite flake tip pushing the layers apart and weakening their attractive force as a function of increased separation distance (demonstrated by the arrows on the graphite tip in (a) and (b1)). **(c1)** Layers overcoming their VdW’s electrostatic attraction break away from the bulk material, as indicated by the red dashed circle. **(b2)** The bubble entrains water in from the back as the depth of the involution increases. Preliminary displacement forces increase the width of the splitting layers, as demonstrated by the arrows on the graphite flake. **(c2)** The collapse after the C-shape also gives rise to a SW. As the bubble rebounds multiple C-shapes and SWs follow thereafter. The bubble collapse points in the diagram demonstrate this tendency, increasing layer separation distance. For clarity, the C-shape is portrayed larger. In reality, by the time the jetting water reaches the opposite side of the cavity wall, the bubble is entering the collapse phase [14,24].

generated between 0.77 and 1.5 mm from the sample), the largest exerting forces (SWs/liquid-jets) were less effective as they did not interact directly along with the stacked inter-graphitic layers (bubble location was normal to the plane surface of graphite) as opposed to the previous cases where bubbles were located along the axis of the graphite layers (Figs. 1 and 2). Instead, the cavitation mechanism observed here focuses on weaker expansion/contraction (oscillating) forces. Specifically, in this case after an initial split occurred at the top of the graphite flake (Fig. (4a),  $497.5 \mu\text{s}$ ) from SW propagation, repetitive growth and collapse bubble phases pushed and pulled the surrounding medium like a pump, leading to layer tearing. Multiple “branches” were formed on the graphite flake that continued

to grow in length as layer tearing propagated due to bubble oscillation. This manifestation is schematically depicted in Fig. 5. In general, the progression of a tear between sheared layers is only really observable during the collapse stage of the cavity as the inertia from the contraction stage pulls the layers apart. Similarly the same contraction/expansion mode can further facilitate the enlargement of the interlayer distance if the bubbles are located in-between the layers as shown in Fig. 2(c2).

Numerical modelling results using bubble parameters from Fig. 4 estimated the alternating compressive/tensile forces in the range  $-35$  to  $+80 \text{ kPa}$  (Fig. S6), apparently adequate to facilitate further propagation of partial exfoliation leading to a “branching”-style formation. Stable cavitation mechanism in

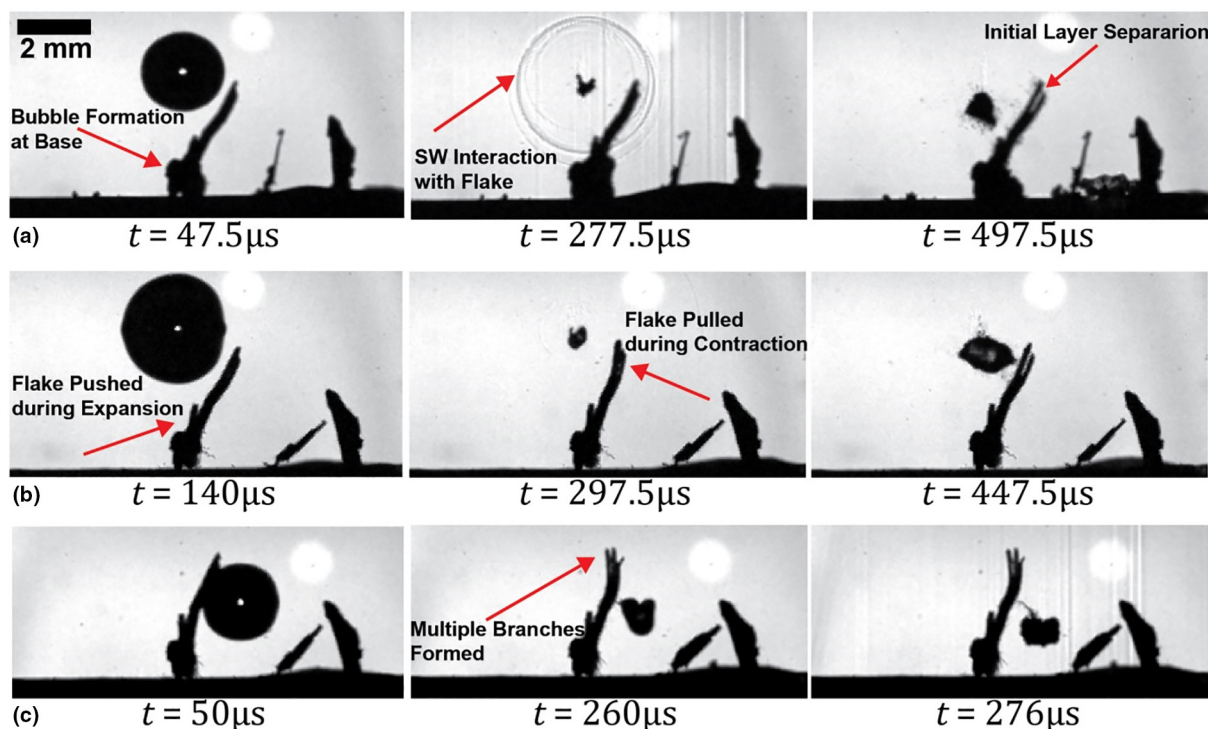


FIGURE 4

Representative frames selected from multiple high-speed sequences recording the interaction of repeated LIBs with a single graphite flake, depicting the “branching” manifestation. Each sequence for each row consists of bubble growth, contraction and collapse. **(a)** Shows the initiation of a split due to a SW interaction (Video 3), with vertical SWs also present due to reflections off the curved mirror. **(b)** Displacement of the graphite flake occurs as it’s pushed away from the bubble during growth, pulled towards during contraction, and during collapse the split becomes evident. **(c)** The bubble implodes from the right hand side with the same phenomenon observable, which becomes more noticeable due to increased number of bubble collapses further propagating the split. The graphite flake is pushed during growth, pulled during contraction and after bubble collapse the full extent of the shearing process is apparent (Video 4). The second image in (c) also displays the cavitation bubble beginning to jet toward the substrate. It is worth noting that the larger width seen at the lower half of the graphite in (a) is due to bubbles stuck at the base.

conjunction with the “branching” manifestation is likely to be the reason why smaller sized bubbles have recently been shown to be more effective in exfoliating graphite flakes [10] (the resonance radius of smaller sized bubbles is associated with high excitation frequencies in the MHz range making it difficult for the bubbles to catastrophically collapse with an incident low frequency source, and as such tend to vigorously pulsate in a stable cavitation manner promoting a “gentler” exfoliation). In addition, this hypothesis is in line with the observations in Section 2.2 (Fig. 7) where bubbles trapped between the graphite layers promoted a gentle and rapid multi-layered exfoliation of a bulk layered graphite flake under continuous sonication.

#### Ultrasonic bubble cloud experiments

Although the use of single bubbles shed light on the dynamics and the governing mechanisms of sono-exfoliation, it is not representative of the continuous dynamic events driven by acoustic cavitation and multiple bubble cloud collapses. Moreover, the fact that the LIBs are particularly large compared to those produced acoustically via ultrasonic excitation, means that a full picture of the underlying mechanisms cannot be assembled. Therefore, the second part of the experiments were performed using a sonotrode in conjunction with acoustic pressure measurements and high speed imaging at lower frame rates (up to 100,000 fps), in order to capture exfoliation under testing and

processing conditions closer to those experienced in ultrasound-assisted LPE. To investigate sono-exfoliation mechanisms under the sonotrode, the experimental setup displayed in Fig. S1(b) was assembled, with the graphite fixed to the substrate at a distance of 1.2 mm or 2.5 mm from the sonotrode tip, in order to observe exfoliation inside and outside the cavitation zone, respectively.

#### Graphite flake: direct cavitation zone interaction

We can now analyse the acoustic cavitation effect of initiating exfoliation of a bulk layered graphite flake. Fig. 6 (a) shows that in the initial  $\sim 3$  ms after the transducer was activated, no cloud is formed. However, after this, the cavitation zone developed to its maximum size for a period of  $\sim 10$  ms (Fig. 6(b-e)). This was found to be a critical processing time as powerful pressure surges, most likely by a train of SWs (as discussed in Supplementary Material Section 3 Fig. S7) directly exerted onto the graphite tip, severed the VdW’s bonds after the first  $\sim 13$  ms of processing. Thereafter a stabilised cavitation regime was achieved (Fig. 6(f)) with the active cavitation zone shrinking to a size about 2.5 times less in area (Fig. 6(f)) than the fully developed case (Fig. 6(c)), indicating reduced cavitation activity and thus a slower exfoliation process. This tendency was also validated by acoustic pressure measurements as shown later in Section 2.3. As there was no direct contact with the graphite during the first

## Exfoliation via Stable Cavitation

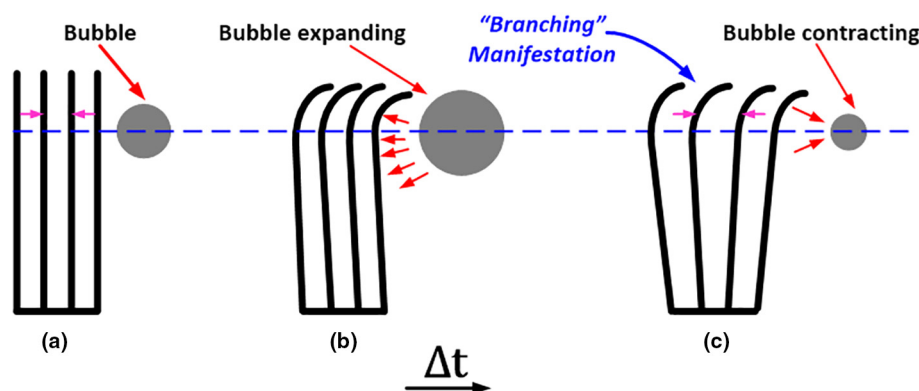


FIGURE 5

Schematic portraying a sono-exfoliation manifestation ("branching") resulting from rapid transitions between bubble growth and contraction, where the output deflection pressures contribute to layered material shearing. **(a)** Shows the initial graphite flake with a forming bubble nearby the tip of the graphite (where each black pillar represents  $\sim 50 \mu\text{m}$  in thickness of graphite). **(b)** Shows the cavitation bubble expanding. The expanding force pushes the closest graphite layers and shears the top layers. **(c)** Shows the bubble contracting. While pulling in the surrounding medium the closest graphite layers are pulled towards the bubble. During this, shearing at the tip of the graphite progresses and hence layer separation distance increases as demonstrated by the pink arrows on the graphite flakes.

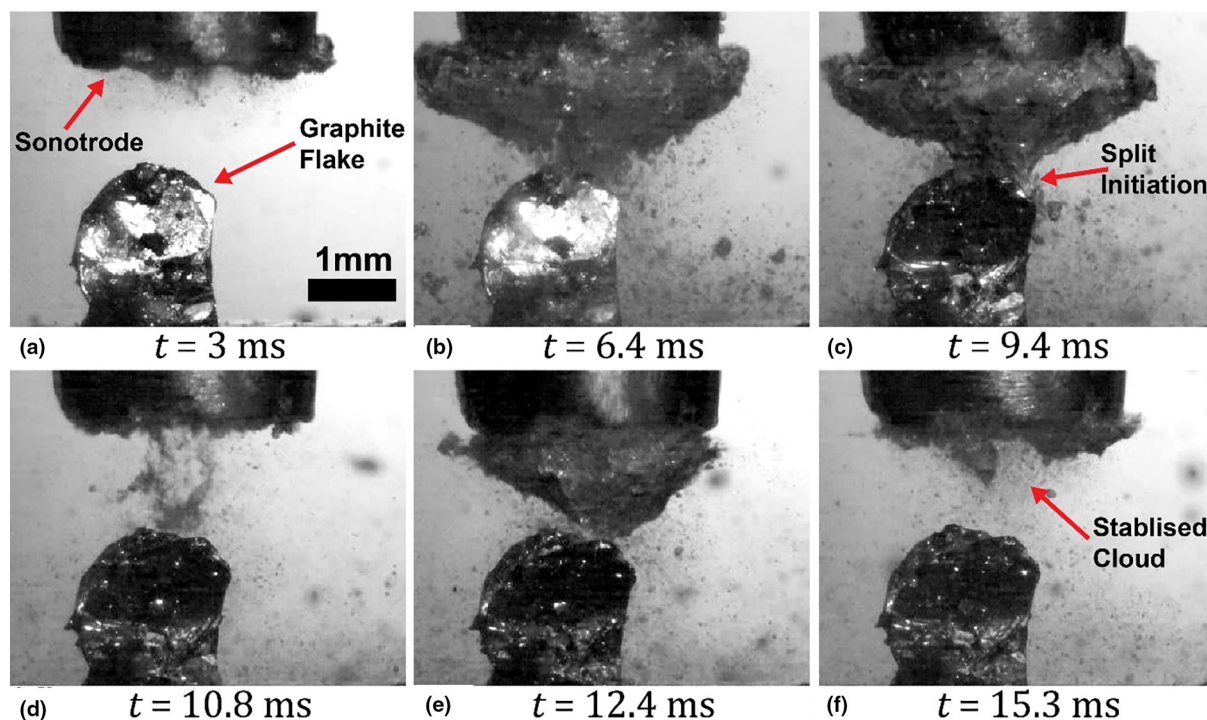


FIGURE 6

Sono-exfoliation via ultrasonic cavitation (single pulse,  $\sim 250 \text{ ms}$  on/ $\sim 750 \text{ ms}$  off). Sequence displaying a cavitation cloud interaction with a graphite flake, splitting the bulk material layers in half. **(a)** Shows the initial morphology of the sample as the sonotrode is activated. **(b)** The cavitation cloud begins to make contact with the graphite flake as the sonotrode tip produces larger bubbly clouds. **(c)** Initiation of the graphite split occurs, with the tip of the cloud remaining in contact. **(d)** The progression of the exfoliating layers continues. The cloud pulse from the sonotrode alternates in size as it oscillates: here we witness weak and dispersed microbubble cloud interactions with the graphite flake. **(e)** Split progression is complete with the cavitation cloud beginning to stabilise, thin and decrease in size. **(f)** Shows no difference in split propagation to the graphite flake. The sonotrode has now normalised in operation, producing a stable and steady bubble cloud which no longer reaches the graphite flake tip, coinciding with the halt of rapid delamination of layers. The corresponding clip for this sequence ([Video 5](#)) alongwith an SEM micrograph of the original and split graphite flake can be found in [Fig. S8](#).



few ms while the sonotrode was seen to oscillate (Video 5), it can be reasonably assumed that the governing exfoliation mechanism is the accumulation of powerful SWs generated from a fully developed cavitation zone interacting with the tip of the graphite flake (Fig. 6(b)).

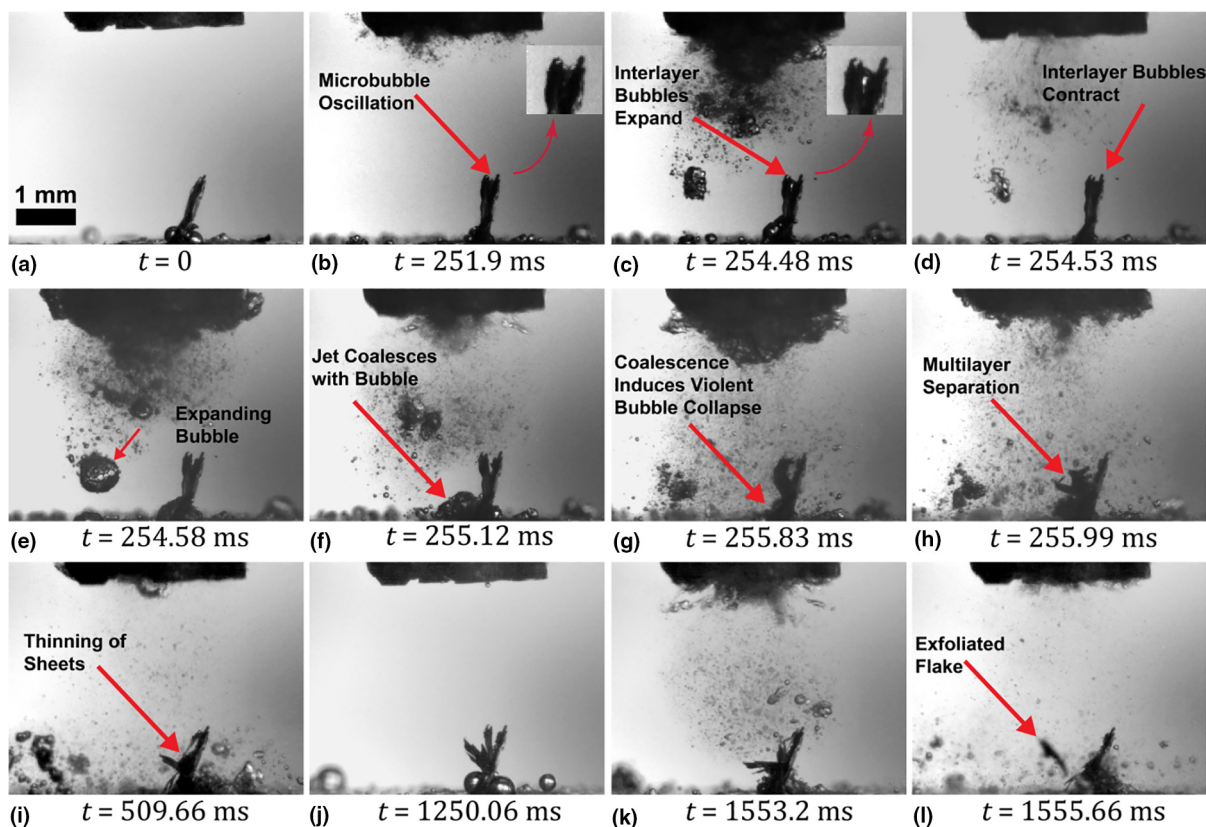
#### Graphite flake: indirect cavitation zone interaction

Fig. 7 displays an ultrasonic experiment with twice the distance ( $\sim 2.5$  mm) between the sample and sonotrode to ensure that the cavitation zone would not interact with the graphite directly. The sample is viewed edge-on from a perspective orthogonal to that of Fig. 6, similar to the LIB observations of Figs. 1–5. The initial split induced (Fig. 7(b)) was similar to what was observed in Fig. 2, where the splitting occurred approximately down the graphite flake centre. Camera observations indicated that bubbles that did not implode could grow in size and sustain an oscillating motion, producing a translational force due to the acoustic pressure field inflicted upon them. Fig. 7(b–d) demonstrated this tendency, whereby smaller bubbles (in the range of  $65\text{--}80\text{ }\mu\text{m}$ ) in-between the split graphite flake layers oscillated rapidly to per-

petuate layer shearing (Video 6). Fig. S9 also presents a schematic of this phenomenon.

Although we cannot directly observe jetting from individual bubbles into the graphite clearly in Fig. 7 due to the multiple bubbles in the solution, we did witness an example of jetting which propelled the liquid mass towards the substrate upon implosion (as observed at 16 s during Video 6). A larger bubble was seen to propagate towards the substrate with periodic implosions (Fig. 7 (e)), at which point a liquid-jet impelled into the base of the graphite, subsequently coalescing and triggering a mass implosion of the stable bubbles already oscillating at the base of the graphite (Fig. 7(f–g)). The bubble implosion along with the generated SWs and micro-jets appeared to coincide simultaneously with multilayer opening from the tip of the graphite (Fig. 7(h)), which occurred 7 periodic bubble collapses after the initial jet interaction with the bubbles at the base of the sample.

Interestingly, the graphite flake opened up in a fashion resembling flipping through pages of a book, prior to the interaction with satellite bubble clouds from the sonotrode. This can be



**FIGURE 7**

Sono-exfoliation via ultrasonic cavitation. The graphite flake was exposed to 7 ultrasonic pulses ( $\sim 250$  ms on/ $\sim 750$  ms off). The sequence consists of selected images highlighting the most interesting phenomena, and does not include every pulse. Images show active treatment, as well as an intermittent period absent of acoustic cavitation. (a) The initial morphology of the sample is shown. (b) Microbubbles oscillate between the split layers at the tip of the graphite (Video 6). (c) Microbubbles expand within the split graphite layers. (d) Microbubbles contract within the split graphite layers. (e) A large bubble expands on the left side of the graphite flake. Meanwhile, the microbubbles in-between the graphite flake split no longer reform. (f) The bubble follows a pathway of continuous contraction and compression phases. A liquid-jet is formed, propelled and coalesces with the stable cavitation at the base of the graphite flake. (g) The coalescence induces a violent collapse separating the graphite layers. (h) Shows multilayer separation of the graphite. (i) Thinning of the graphite sheets becomes more noticeable. (j) Displays a still shot while the sonotrode has not yet produced acoustic cavitation. The larger exfoliating graphite sheets transform into smaller sub-sheets continuing to tear further towards the base of the graphite flake. (k) The multiple exfoliating layers are inflicted by inertial cavitation and acoustic streaming forces. (l) Exfoliation occurs. A small section is seen to fully sever from the bulk graphite and proceeds to flow around the solution (Video 7).



clearly seen in [Video 6](#), [Fig. 7\(f-h\)](#), and depicted in [Fig. S10](#). To the best of our knowledge, this phenomenon was observed here for the first time demonstrating that graphite flake layers can separate and displace similar to book pages, with multiple partially exfoliated graphite layers (still bound by VdW's bonds at the lower half of the sample) being able to move fluidly during the interaction with cavitating bubbles and corresponding acoustic emissions.

It was recently shown that bubble implosions near a rigid solid boundary generate shear stresses in the range of up to 100 kPa [25] upon liquid-jet impact with corresponding SWs impact pressures in the range of 1–2 MPa [26] (for a distance of about 200  $\mu\text{m}$ , comparable to the studied bubble i.e. [Fig. 7\(e\)](#),  $\sim 300 \mu\text{m}$ ). [Fig. 7\(e-g\)](#) shows a visual representation of this phenomenon, whereby bubble implosions can be promoted by nearby solid boundaries. These values are in very good agreement with our measured and calculated pressure values given in Section 2.3. The most pertinent information from Section 2.2 is that the combination of the generated SWs, micro-jets and bubble oscillations each imposed shear stresses onto the graphite flake along with acoustic streaming, leading to “page-flipping” exfoliation. Thus, the next step was to map and resolve the pressure magnitude of these acoustic emissions in the sonicated environment and estimate the shear stresses responsible for the exfoliation. [Fig. 7\(i\)](#) demonstrates the thinning of separated graphite layers followed by an intermittent sonication period ([Fig. 7\(j\)](#)) where the graphite flake resembled the “flowering” manifestation, with an expanding tip surface area and separation distance. The subsequent ultrasonic pulse exfoliated a graphite flake section ([Fig. 7\(k-l\)](#)) of  $\sim 650 \mu\text{m}$  in length,  $\sim 520 \mu\text{m}$  width and  $\sim 30 \mu\text{m}$  in thickness ([Video 7](#)).

It was also observed in [Fig. 7\(b, c\)](#) that during the first  $\sim 3 \text{ ms}$  after the transducer was activated, the graphite flake could be seen to vibrate in response to sonotrode tip vibration, in the absence of bubble collapse SWs. The next  $\sim 10 \text{ ms}$  gave rise to a rapidly growing cavitation cloud with increasing aggressiveness, followed by shrinking to a stabilised cavitation zone, with rapid layer exfoliation no longer observed. This phenomenon was observed for both [Fig. 6](#) using a single pulse, and [Fig. 7](#) using seven pulses of ultrasound. Each pulse delivered to the graphite flake observed with the camera, demonstrated proliferation of layer delamination specifically during the  $\sim 10 \text{ ms}$  cavitation cloud expansion, and hence provides visual evidence for the utility of short pulsed ultrasound for exfoliation.

Pulsed, as opposed to continuous ultrasound has been reported to reduce energy usage, ensure better temperature control and prevent reactor clogging [27]. It has been proposed that pulsed ultrasonic treatment facilitates and promotes the generation of cavitation by utilising the silent period during which the liquid medium is not treated [28], hence promoting nuclei replenishment. It was also hypothesised that generation of greater number of transient cavitation occurs due to increased nucleation sites [29]. However, these hypotheses have never been experimentally confirmed before. In this research, photographic evidence along with acoustic pressure measurements ([Fig. 8](#)) revealed the foundation for the benefit of using pulsed ultrasound for treatment of graphite solutions.

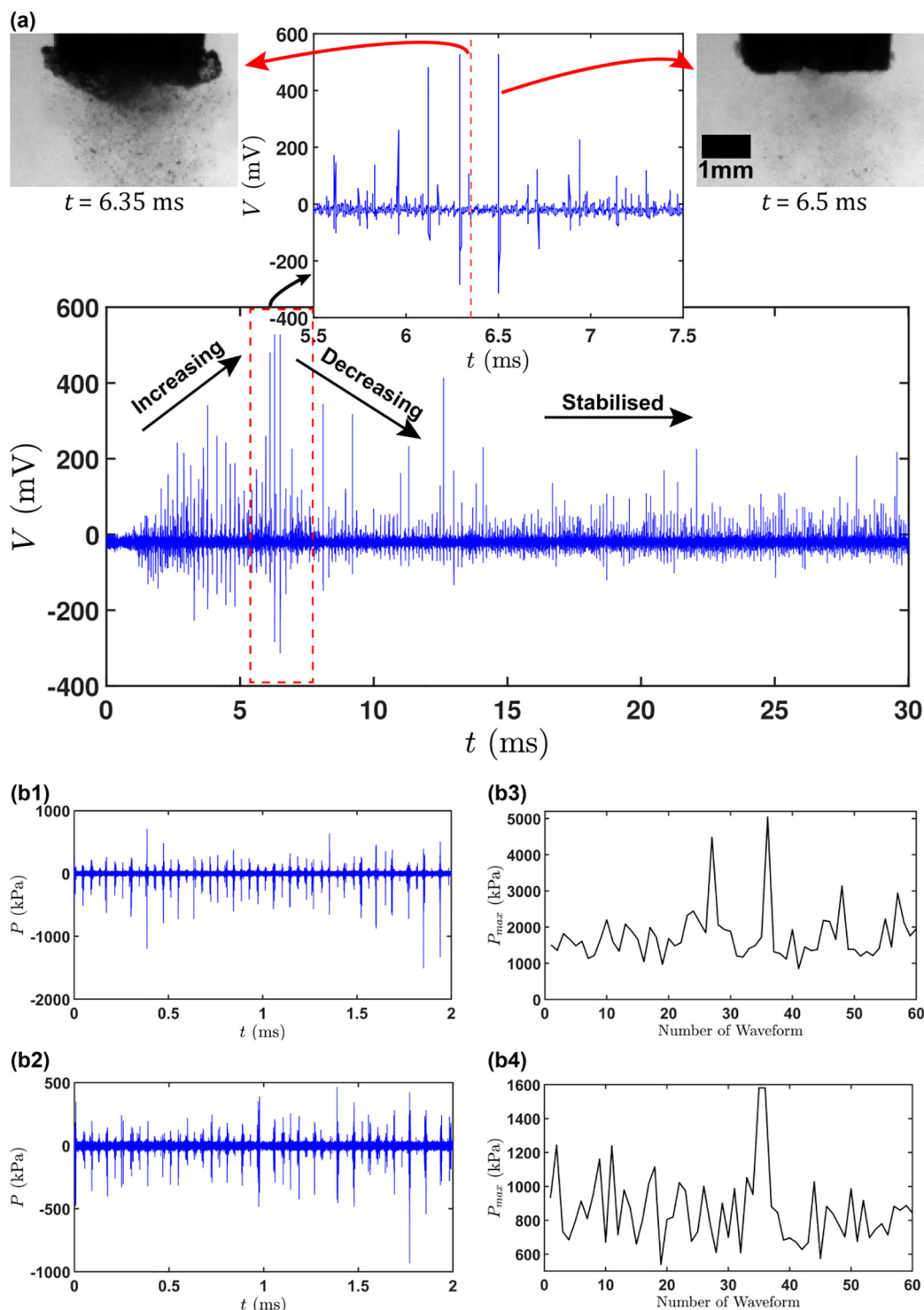
### Acoustic pressure measurements and calculation of cavitation induced shear stresses

In general, the collapse of a larger bubble cloud (many collapses of individual cavitating bubbles) produces larger force exerted due to increased acoustic emissions. [Fig. 8\(a\)](#) presents additional evidence to the hypothesis made in Section 2.2 that a proliferation of layer tearing occurred during the initial sonication period ( $\sim 13 \text{ ms}$ ). The cavitation intensity can be seen to increase until  $\sim 7 \text{ ms}$ . Due to the fibre optic hydrophones flexibility to prevent breaking, the position of its tip displaced (increasing distance from the sonotrode) under the growing emissions from the cavitation cloud, and hence the recorded signal appeared to decrease. However, as observed from the camera recording in [Figs. 6 and 7](#), this would most likely increase until  $\sim 13 \text{ ms}$ . The fibre optic hydrophone synced to the high-speed camera ([Fig. 8\(a\)](#)) allows us to authenticate the supposition made in the previous section. The image at 6.35 ms showed a fully developed bubble cloud. At 6.5 ms the image showed the collapse of the cloud, which appeared to coincide precisely to the large peak in signal. The collapse of this large cloud was likely to have released multiple SWs due to transient bubble collapses (seen [Fig. S7](#)) which expedited the exfoliation of graphite layers. The latter half of the plot in [Fig. 8\(a\)](#) showed a stabilisation of the acoustic emissions, with much lower signals observed (about 3 times), reflecting a smaller cavitation zone.

The profile of acoustic pressure surges for a stabilised cavitation zone from SWs at the studied locations is given in [Fig. 8 \(b\)](#) (the full pressure map of the active cavitation zone along with more detail can be found in [Fig. S11](#)) using the methodology previously used by our group [30,31]. Maximum pressure ( $P_{\text{max}}$ ) readings (averaged from 60 waveforms in [Fig. 8\(b3-4\)](#), corresponding to 120 ms) were measured as 1770 and 860 kPa for graphite sample positions in [Figs. 6 and 7](#), respectively. However, SW pressure impacts at particular waveforms such as 28 and 35 ([Fig. 8\(c-d\)](#)) reached values up to 5 MPa (at 1.2 mm) and 1.6 MPa (at 2.5 mm), respectively. These local maxima correspond to the accumulated pressures peaks generated in [Fig. 8 \(a\)](#), where the cavitation zone reaches maximum size. It is apparent that during the first 10 ms the accumulated pressure surges ([Fig. 8\(a\) inset](#)) facilitated exfoliation as also seen in [Figs. 6 and 7](#). Most other waveforms during a stabilised regime measured lower pressure values between 1–2 MPa. These measured values are in good agreement with the calculated shear stress values required to separate graphite layers apart, as per discussion below in this Section and experimentally measured in macroscale experiments [32], however, they are much lower than those given in [Table 1](#) and calculated using the double cantilever beam (DCB) formula ([Supplementary Material Section 5, Eq. S1](#)).

The DCB formula estimates the total force delivered to the graphite flake tip from the collapsing bubbles. From the values in [Table 1\(a\)](#) it is apparent that shearing pressures for [Fig. 2](#) (splitting induced from LIB jetting) and 6 (splitting induced from acoustic cavitation) are close in value.

To the best of our knowledge, quantifying sufficient shearing pressures to enact layer delamination brings about widely disputed and varying values, mostly due to the complexities of accurate measuring, variety of measurement techniques, and a

**FIGURE 8**

(a) Cavitation intensity plot for 2.5 mm distance from the sonotrode (as in Fig. 7). The zoomed dashed red box section highlights the initial sonication period where the largest signal is detected by the fibre-optic hydrophone. The image at 6.35 ms shows a fully developed bubble cloud. The image at 6.50 ms shows the collapse of this cloud, which corresponds to the large voltage peak. The black arrows on the main plot demonstrate the stabilisation of the trend/signal after  $\sim 13$  ms as mentioned in section 2.2. (b) Temporal distribution of shock wave pressure: (b1) for sample in Fig. 6 and (b2) for sample in Fig. 7. These plots represent the first recorded waveform for each instance after bubble cloud stabilisation. The total pressures were averaged from 60 generated waveforms. (b3) and (b4) show the 60 recorded points against maximum pressure for corresponding cases (b1) and (b2) respectively.

multitude of parameters which are challenging to control. Therefore, a lack of reproducibility is often the case. One metrology which holds up as a reasonable estimate for exfoliation is the interlayer shear strength (ISS). Liu et al. pointed out the large dis-

crepancies of calculated ISS values of graphite that were between 0.2 MPa and 7 GPa [32]. At the same time, they stated that much smaller ISS values in the range of 0.25 to 2.5 MPa were attributed to the existence of many incommensurate contacts, which could

TABLE 1

**Pressure estimates for (a) graphite split, and (b) deflection. Data and calculations are provided in the Supplementary Material Section 5.**

(a) Double Cantilever Beam Impact Pressures (MPa) (Eq. S1)	
Fig. 2	54 to 557
Fig. 6	66 to 677
(b) Deflection Impact Pressures (MPa) (Eq. S2)	
Fig. 2(a2)- Expansion	2–21
Fig. 2(a2)- Contraction	0.7–7
Fig. 4- “Branching” Expansion	0.2–9
Fig. 4- “Branching” Contraction	0.2–6

significantly reduce the shear strength because of the superlubricity of non-pristine graphite.

Pressure estimates calculated via the DCB formula for graphite shearing (Table 1(a)) are greater than the reported SW pressures in the range of 4–11 MPa (at a distance of 3 mm from the bubble centre) for LIB [33], as well as those measured with the fibre optic hydrophone in a sonicated environment. The calculated values of graphite shearing using DCB were, however, taken for samples with perfect integrity, without flaws/defects and cracks. Therefore, providing sufficient shearing would require a greater force as opposed to non-pristine graphite flakes (see Fig. S8). The fibre optic hydrophone measurements provided evidence that non-pristine graphite VdW's bonds can separate under much lower pressure impacts (we observed a range of ~0.7–5 MPa for cases Fig. 8(b3-b4), with periodic pressure bursts from ~50 SWs in 2 ms from the sonotrode tip during sonication), which aligns with Liu's lower range of ISS measurements [32]. We can then hypothesise that graphite splitting and exfoliation mechanisms likely resemble a low cycle fatigue process by accumulating pressures, whereby the accumulation of SWs with pressure surges generally dismantle the VdW's bonds in due time (less than 13 ms for the studied samples positioned in plane with the VdW's bonds). Moreover, the contribution of micro-jets, acoustic streaming and cavitation expansion/contraction further provide the necessary shearing forces as explained with more detail in Fig. S10.

Deflection pressures calculated for the expansion cavitation bubble phase (Eq. S2) for the case shown in Fig. 2(a2) where the bubble imploded directly over the split were greater than those exerted onto the graphite flake in the case shown in Fig. 4 where the bubble oscillated on the side of the flake (Table 1). This difference was due to the bubble positioning which expedited the progression of inter-layer tearing as bubble expanding forces emitted were inflicted directly over the pre-split graphite flake in the case of Fig. 2. Due to this positioning, the expanding bubble appeared to promote efficacy of layer tearing, as it corresponded in plane to VdW's bonding. The contracting bubble in Fig. 2(a2) produced significantly reduced deflection pressures (about three times from Eq. S2), such that a contracting bubble in this location is less beneficial in terms of layer tearing (Video 2). Bubble oscillating pressures from earlier research are shown to be between 0.1–0.5 MPa [23], coinciding with the lower range of values in Table 1(b). By analysing the graphite flake in Fig. 4, the deflection pressures produced by bubble expansion were calculated in the range of 0.2–9 MPa, while the deflection pressures for bubble contraction were in the range of

0.2–6 MPa (Table 1(b); calculations can be found in Supplementary Material Section 5, using Eq. S2). Therefore, no salient difference can be ascertained between the forces emitted as a consequence of either cavitation expansion or contraction. The larger values calculated for bubble expansion were attributed to larger graphite flake deflection, which in turn produced greater impact pressures. However, the camera observation (Fig. 4(b-c)) indicated that bubble compression in this position mainly facilitated layer tearing, as pulling apart the layers helped to overcome their VdW's bonds via separation distance, as opposed to simply pushing layers together during rarefaction. However, this is not the case for bubbles that are already entrapped within the layers, whereby expansion seems to promote further opening of the graphite layers as observed in Fig. 7(b-d), and similar to Fig. 2 (b) mentioned above (although that instance was a single bubble above the split) and explained in Fig. 5. Thus, we can certainly say that, depending on the position of the bubbles, an efficient synergetic mechanism based on the location of stable oscillating bubbles can be established. In our earlier research we suggested that the small-size bubbles excited by MHz frequencies can penetrate the thin layers of the graphite, grow in due time and increase the inter-layer spacing in a gentle fashion, while simultaneously, larger bubbles excited by kHz frequencies and located at the outer vicinity of the graphite can pull the layers further apart during their contraction [10]. This synergy can be instrumental in optimising and advancing the sono-exfoliation process. Section 6 in Supplementary Material and Fig. S12 include a proposed ultrasonic setup taking into account our experimental observations, acoustic pressure readings and guidelines on the technological implementation of the findings of this study.

## Conclusions

This study presents the first ever recorded evidence of graphite exfoliation using cavitation bubbles. Phenomenological descriptions from the experiments uncovered various mechanisms and manifestations, which contribute to the exfoliation of graphite when subjected to laser induced single-bubble cavitation or acoustic cavitation. We demonstrated that the entire process of ultrasonic exfoliation of graphite is more complicated than previously thought.

Using high-speed imaging four specific manifestations of “flowering”, “slicing”, “splitting” and “branching” driven by the two main mechanisms of transient and stable cavitation were identified and demonstrated to be essential contributing factors to graphite exfoliation. Analysis of the high-speed imaging data proved that SW impacts alone are sufficient to initiate the exfoliation process as well as facilitate delamination of the graphite layers. The observations showed how cavitation bubble collapses can firstly increase the graphite flake surface area, followed by slicing and peeling. Moreover, micro-jets were seen to produce liquid mass entrainments that split layers effectively, while expanding and contracting forces emitted by oscillating (stable) cavitating bubbles also contributed to the exfoliation process.

Accumulated SW pressures in the range of 0.7–5 MPa are sufficient for exfoliation of the studied graphite flakes. In addition, acoustic streaming is seen to aid in the dispersion of LPE, as well as promoting bubble migration to the interlayers, and providing



additional layer separating forces, where stable oscillating microbubbles nucleating between the split layers lead to “page-flipping” exfoliation. Finally, evidence for the utility of pulsed ultrasonic waves for exfoliation was presented. The short initial period of 10 ms (for our sonotrode) where the cavitation cloud grows was shown to proliferate layer tearing.

The aforementioned sono-exfoliation mechanisms and manifestations provide direct and solid evidence of the fundamental proclivity of layer material exfoliation under cavitation. As a result, the reported data can be instrumental for developing a large scale, environmentally friendly ultrasound based liquid exfoliation process; and can be directly applied to the validation and development of relevant sono-exfoliation numerical models that are required for optimisation and control of ultrasonic exfoliation processing.

## Method

### *Laser induced bubble experimental setup-*

The source material used was Sigma-Aldrich graphite flakes of approximately 149  $\mu\text{m}$  in size (mesh 100). These were fixed vertically onto a metallic holder with a cyanoacrylate adhesive, which was then lowered and positioned into a custom-built chamber ( $420 \times 438 \times 220 \text{ mm}^3$ ) on a translational stage filled with degassed and deionised water. The main components of the LIB set up included the pulsed laser, immersed parabolic mirrors, camera and synchronous illumination source as illustrated in Fig. S1(a). The full apparatus setup and schematic can be found elsewhere [19].

The water temperature was at ambient conditions (25 °C) and did not alter due to the generation and collapse of individual bubbles (because the duration of experiments was short). The design of the cavitation chamber allowed for precise image observation to capture the position of the LIB and the graphite flake.

A 6–8 ns laser-pulse was generated from 532 nm irradiation (Litron TRL 420-10 Q-switched frequency-doubled Nd:YAG), whereby the pulse was brought into focus through a curved mirror (Silver-Coated Concave Mirror,  $f = 19.0$ ) and a macro-lens, which was used to provide imaging for the camera (Milvus 147 100 mm  $f/2M$ , Zeiss, Oberkochen, Germany). Laser power was between 10 and  $88.8 \text{ mJ} \pm 10\%$  (instrumental error) sufficient to generate elliptical plasma regions that rapidly expanded to form approximately spherical cavitation bubbles. The generated bubbles were within the range of  $\sim 0.8$ – $1.4 \text{ mm}$  in radius at maximum inflation, experiencing between a  $\sim 0.18$  and  $0.3 \text{ ms}$  life-cycle period before initial collapse. These bubbles generally underwent 3–4 rebound oscillation cycles.

Films were captured by high-speed shadowgraphic imaging using a Shimadzu (HPV X2) camera at a frame rate of 400,000 fps, with a resolution of  $400 \times 250$  pixels, generating 256 frames for every recorded sequence. Synchronised 10 ns laser pulses through a collimating lens provided the illumination (CAVILUX Smart UHS system) and effective temporal resolution to observe the generated SWs.

### *Ultrasonic probe experimental setup-*

Graphite source and sample setup was the same as mentioned above for the LIB experiment. This time a rectangular  $7.5 \times 10 \text{ cm}$  glass chamber filled with deionised water (Hexeal

chemicals) was used for measurements. The tank temperature remained ambient at 25 °C without the need of a temperature controller device due to using only short ultrasonic pulses ( $\sim 250 \text{ ms}$ ) initiated from the sonotrode.

A Hielscher UP200S system with a 3 mm diameter titanium sonotrode and an operational frequency of 24 kHz was used to initiate cavitation. The peak-to-peak amplitude was set to 42  $\mu\text{m}$ , corresponding to an operating power of 40 W, and used in a 25% pulse mode ( $\sim 250 \text{ ms}$  on/ $\sim 750 \text{ ms}$  off). The radiating surface of the vertically mounted sonotrode was immersed 55–57 mm below the liquid surface.

High-speed imaging was carried out using a Photron- SA-Z 2100K camera at a frame rate of 100,000 fps over  $640 \times 280$  pixels, at a resolution of  $12.7 \mu\text{m/pixel}^{-1}$  and a shutter speed of 8.39  $\mu\text{s}$ . Illumination was provided by a powerful front light beam LED flash lamp (GS Vitec). Fig. S1(b) shows a schematic of the experimental setup.

Within the scope of our study, the size and shape of graphite flakes used did not affect the mechanisms observed with in situ observations (see Table 1).

### *Acoustic pressure measurements and data acquisition*

A fibre-optic calibrated hydrophone system (Precision Acoustics Ltd) was used to measure the acoustic pressure emissions to which the graphite flakes were exposed, generated by cavitating bubbles and bubbly clouds via a sonotrode. The hydrophone was calibrated between 1 and 30 MHz thus only the pressure exerted from SWs could be captured and analysed as they lie within this frequency range [31]. The fibre-optic sensor was located at a distance of 1.2 and 2.5 mm from the tip of the sonotrode corresponding to the graphite flake position. These locations were chosen as they demonstrated a range where rapid exfoliation took place (up to 3 mm), including examples of both direct and indirect cavitation cloud interactions with the graphite flake, and being prime examples of the exfoliation mechanisms taking place. The pressure measurements were captured via a digital oscilloscope (Picoscope 3000 series) connected to the hydrophone and 60 waveforms of cavitating emission signals were recorded and averaged. The corresponding readings were converted to spectra using fast Fourier transform over a 2-ms time period as previously shown elsewhere [31,34]. The conversion process was used to calculate the maximum pressure ( $P_{\text{max}}$ ) values from the hydrophone output voltage, and also intrinsic background noise was removed during this stage, by means of subtraction from the initial voltage signal.

### *Multiphysics modelling*

The VOF method was used to track the bubble (primary phase) surface dynamics in water (secondary phase), assuming that the phases are not interpenetrating. The two phases are considered compressible. The continuum surface force (CSF) model was used to describe the effect of surface tension in the VOF model. The Reynolds averaging method (RANS) was used to handle turbulence in the flow field. The RANS method is based on the Navier-Stokes (N-S) equation, and introduces the Reynolds hypothesis to formulate the Reynolds-time N-S equation. Further details about these models can be found in the references elsewhere [35,36].

Using bubble parameters (bubble diameter and distance from the graphite flake) from the single LIB experiments, simulations were developed to estimate SW impacts and bubble oscillation pressures. These simulations and estimates are to serve as an indication to the magnitude of forces emitted onto the graphite flake in each case of manifestation.

### Data availability

The data that supports the findings of this study are available upon request from the corresponding author.

### CRediT authorship contribution statement

**Justin A. Morton:** Conceptualization, Methodology, Writing - original draft, Writing - review & editing, Visualization. **Mohammad Khavari:** Software, Visualization, Writing - review & editing. **Ling Qin:** Methodology, Software, Writing - review & editing. **Barbara M. Maciejewska:** Resources, Writing - review & editing. **Anastasia V. Tyurnina:** Writing - review & editing. **Nicole Grobert:** Writing - review & editing, Funding acquisition. **Dmitry G. Eskin:** Writing - review & editing, Funding acquisition. **Jiawei Mi:** Writing - review & editing, Funding acquisition. **Kyriakos Porfyrakis:** Writing - review & editing, Funding acquisition. **Paul Prentice:** Resources, Writing - review & editing. **Iakovos Tzanakis:** Supervision, Conceptualization, Writing - review & editing, Funding acquisition.

### Acknowledgements

This work has been funded by the UK Engineering and Physical Sciences Research Council (EPSRC), to the project “Sustainable and industrially scalable ultrasonic liquid phase exfoliation technologies for manufacturing 2D advanced functional materials” (EcoUltra2D), with the grant nos. EP/R031665/1; EP/R031401/1; EP/R031819/1; EP/R031975/1. NG also thanks the Royal Society for financial support.

### Appendix A. Supplementary data

Supplementary data to this article can be found online at <https://doi.org/10.1016/j.mattod.2021.05.005>.

### References

- [1] K.S. Novoselov et al., *Science* 306 (5696) (2004) 666–669, <https://doi.org/10.1126/science.1102896>.
- [2] A.K. Geim, *Science* 324 (5934) (2009) 1530–1534, <https://doi.org/10.1126/science.1158877>.
- [3] A.A. Balandin et al., *Nano Lett.* 8 (3) (2008) 902–907, <https://doi.org/10.1021/nl0731872>.
- [4] K.I. Bolotin et al., *Solid State Commun.* 146 (9–10) (2008) 351–355, <https://doi.org/10.1016/j.ssc.2008.02.024>.
- [5] H. Tao et al., *Phys. Chem. Chem. Phys.* 19 (2) (2017) 921–960, <https://doi.org/10.1039/c6cp06813h>.
- [6] Z. Sun et al., *Adv. Sci.* 12 (1) (2019) 1–34, <https://doi.org/10.1002/adv.201901084>.
- [7] K. Khan et al., *J. Mater. Chem. C* 8 (2) (2020) 387–440, <https://doi.org/10.1039/C9TC04187G>.
- [8] V. Nicolosi et al., *Science* 340 (2013) 6139, <https://doi.org/10.1126/science.1226419>.
- [9] Y. Xu et al., *Nanomaterials* 8 (11) (2018) 942, <https://doi.org/10.3390/nano8110942>.
- [10] A.V. Tyurnina et al., *Carbon N. Y.* 168 (2020) 737–747, <https://doi.org/10.1016/j.carbon.2020.06.029>.
- [11] P. Turner et al., *Sci. Rep.* 9 (1) (2019) 1–8, <https://doi.org/10.1038/s41598-019-45059-5>.
- [12] N.K. Bourne, J.E. Field, *J. Fluid Mech.* 244 (1992) 225–240, <https://doi.org/10.1017/S00222112092003045>.
- [13] M. Dular et al., *Wear* 257 (11) (2004) 1176–1184, <https://doi.org/10.1016/j.wear.2004.08.004>.
- [14] I. Tzanakis et al., *Ultrason. Sonochem.* 21 (2) (2014) 866–878, <https://doi.org/10.1016/j.ulsonch.2013.10.003>.
- [15] K. Muthoosamy, S. Manickam, *Ultrason. Sonochem.* 39 (2017) 478–493, <https://doi.org/10.1016/j.ulsonch.2017.05.019>.
- [16] G. Zhou et al., *Sci. Rep.* 8 (1) (2018), <https://doi.org/10.1038/s41598-018-35008-z>.
- [17] W. Hentschel, W. Lauterborn, *Appl. Sci. Res.* 38 (1) (1982) 225–230, <https://doi.org/10.1007/BF00385952>.
- [18] B. Gerold et al., *Rev. Sci. Instrum.* 82 (4) (2011) 044902, <https://doi.org/10.1063/1.3579499>.
- [19] K. Johansen et al., *Ultrasonics* 73 (2017) 144–153, <https://doi.org/10.1016/j.ultras.2016.09.007>.
- [20] M. Yi, Z. Shen, *J. Mater. Chem. A* 3 (22) (2015) 11700–11715, <https://doi.org/10.1039/C5TA00252D>.
- [21] Y. Kawanami et al., *Therm. Eng.* 45 (3) (2002) 655–661, <https://doi.org/10.1299/jseeb.45.655>.
- [22] T. J. C. Van Terwisga, P. A. Fitzsimmons, L. Ziru, and E. J. Foeth, “Cavitation Erosion – A review of physical mechanisms and erosion risk models,” in *Proceedings of the 7th International Symposium on Cavitation*, 2009, no. 41, pp. 1–13.
- [23] T.H. Kim, H.Y. Kim, *J. Fluid Mech.* 750 (2014) 355–371, <https://doi.org/10.1017/jfm.2014.267>.
- [24] I. Tzanakis, M. Hadfield, I. Henshaw, *Exp. Therm. Fluid Sci.* 35 (8) (2011) 1544–1554, <https://doi.org/10.1016/j.expthermflusci.2011.07.005>.
- [25] Q. Zeng et al., *J. Fluid Mech.* 846 (2018) 341–355, <https://doi.org/10.1017/jfm.2018.286>.
- [26] Y.A. Pishchalnikov et al., *J. Acoust. Soc. Am.* 146 (1) (2019) 516–531, <https://doi.org/10.1121/1.5116693>.
- [27] C. Delacour, C. Lutz, S. Kuhn, *Ultrason. Sonochem.* 55 (2019) 67–74, <https://doi.org/10.1016/j.ulsonch.2019.03.012>.
- [28] M. Ashokkumar, *Ultrason. Sonochem.* 18 (4) (2011) 864–872, <https://doi.org/10.1016/j.ulsonch.2010.11.016>.
- [29] V. Ciaravino, H.G. Flynn, M.W. Miller, *Ultrasound Med. Biol.* 7 (2) (1981) 159–166, [https://doi.org/10.1016/0301-5629\(81\)90005-3](https://doi.org/10.1016/0301-5629(81)90005-3).
- [30] A. Priyadarshi et al., *Ultrason. Sonochem.* 70 (2021) 105260, <https://doi.org/10.1016/j.ulsonch.2020.105260>.
- [31] M. Khavari et al., *J. Fluid Mech.* 186 (2021), <https://doi.org/10.1017/jfm.2021.186>.
- [32] Z. Liu et al., *Acta Mech. Sin. Xuebao* 28 (4) (2012) 978–982, <https://doi.org/10.1007/s10409-012-0137-0>.
- [33] G. Sinibaldi et al., *Phys. Fluids* 31 (10) (2019) 103302, <https://doi.org/10.1063/1.5119794>.
- [34] G.S.B. Lebon et al., *Ultrason. Sonochem.* 42 (2018) 411–421, <https://doi.org/10.1016/j.ulsonch.2017.12.002>.
- [35] P. Koukouvinis et al., *Phys. Fluids* 28 (5) (2016) 052103, <https://doi.org/10.1063/1.4949354>.
- [36] P. Koukouvinis et al., *Phys. Fluids* 28 (3) (2016) 032110, <https://doi.org/10.1063/1.4944561>.